Ionosphere Monitoring Methodology for Hybrid Dual-Frequency LAAS

Hiroyuki Konno, Sam Pullen, Jason Rife, and Per Enge
Stanford University

ABSTRACT

Strong ionosphere storms are a potential threat for the Local Area Augmentation System (LAAS). During these storms, very large spatial gradients of ionosphere delays might cause significant errors in user position estimation. Therefore, LAAS needs to continuously monitor ionosphere behavior in order to ensure integrity against the ionosphere anomalies.

This paper introduces a new ionosphere monitoring method using dual-frequency GPS signals. This method consists of two algorithms, each of which measures a different aspect of the ionosphere delay behavior. The first algorithm estimates the rate of change of the ionosphere delay in time by using dual-frequency carrier-phase measurements. Although the algorithm estimates the temporal gradients very precisely, it cannot observe ionosphere fronts which appear to be stationary. The second algorithm directly computes the ionosphere spatial differences between the LAAS Ground Facility (LGF) and the user, estimating the ionosphere delays with dual-frequency code measurements. By definition, this algorithm has no unobservable condition. However, the estimated differences are noisy.

Combining these two algorithms, we develop an ionosphere monitoring method in which these algorithms work complementarily. We then formulate a theoretical Vertical Protection Level (VPL) customized to this method. Availability simulations show that the system with the new monitor provides better performance than conventional single-frequency LAAS.

1. INTRODUCTION

Local-area differential GPS systems such as the Local Area Augmentation System (LAAS) assume near-perfect correlation of the ionosphere delays between LGF and users. However, large spatial gradients during strong ionosphere storms can invalidate this basic assumption and cause hazardous errors in user position estimations [1,2]. Hence, severe ionosphere anomalies are a potential threat to LAAS that, while rare, must be mitigated to a significant degree to support Category III (CAT III) precision landings in the future.

Dual-frequency GPS techniques are know to be an effective means to reduce or remove ionosphere-induced errors and thus improve the robustness of LAAS to ionosphere anomalies [3,4,5]. In a previous study [3], we selected two dual-frequency methods and evaluated their effectiveness under anomalous ionosphere conditions. These methods were divergence-free smoothing (denoted here as “DFree”) and ionosphere-free smoothing (denoted here as “IFree”). Simulations showed that, if the system had perfect knowledge of the ionosphere status in real-time, DFree provided much better availability than IFree for most ionosphere conditions, whereas IFree was superior only under extremely anomalous conditions. This result suggested that optimal system availability would be obtained by using DFree for nominal or moderately anomalous conditions and switching to IFree under extremely anomalous conditions (i.e., conditions that otherwise would be the most hazardous to users). We named this system “hybrid dual-frequency LAAS”.

An important problem remained from the earlier study: how does the system monitor the ionosphere status? Without an ionosphere monitor, the hybrid system cannot appropriately change the primary method from DFree to IFree in real time. Moreover, because DFree cannot mitigate all hazardous ionosphere conditions, an ionosphere monitoring is necessary for DFree to meet the stringent integrity requirement of CAT III landings. Hybrid dual-frequency LAAS can ensure the integrity against ionosphere anomalies by using the monitor to exclude threatening satellites, to inflate user error bounds in real-time, or to trigger a switch between DFree and IFree.

In this paper, we introduce a method to monitor the ionosphere behavior between LGF and users using dual-frequency GPS. This method consists of two algorithms which measure different aspects of ionosphere

delay. The first algorithm measures the rate of change of ionosphere delay over time using dual-frequency carrier-phase measurements. Previous studies [6,7] have introduced various methods to estimate temporal gradients using both L1 code and carrier measurements together. In contrast with these methods, the proposed algorithm uses only carrier measurements to estimate temporal gradients very precisely with a simple noise reduction filter.

On the other hand, this algorithm shares a common problem with other methods: it does not directly measure the ionosphere spatial gradients (or differences) between LGF and users. To evaluate the performance of the algorithm, the observed temporal gradients need to be converted to the equivalent spatial gradients. For the mapping, we use a conventional model which assumes that a temporal gradient result from motion of an ionosphere-pierce-point (IPP) through a linear ionosphere spatial gradient (the linear gradient is conventionally called an "ionosphere front"). Given this mapping model, this algorithm cannot observe a particular ionosphere condition in which a large spatial gradient "synchronizes" with an IPP; i.e., it moves in the same direction and the same speed as the IPP. Analyzing the movement of IPPs for several airports in the United States, we have concluded that the algorithm can, in practice, detect all ionosphere fronts simultaneously affecting three or more satellites. Hence, the critical condition for the DFree LAAS with this monitoring algorithm is a severe ionosphere front simultaneously affecting two satellites without being detected by the monitor.

To compensate for this undetectable condition, we introduce the second algorithm. This algorithm directly computes ionosphere spatial differences from the ionosphere delays at the LGF and user. These delays are computed using dual-frequency code measurements. This algorithm has no undetectable condition; however, the use of the code measurements on two frequencies induces two problems. One is the inter-frequency bias (IFB) [8,9] and the other is a high amount of noise. To eliminate the IFB, we take the *double difference* of the delays. To reduce the noise, we apply a carrier-smoothing filter with a long time constant.

Combining these two algorithms gives an ionosphere monitor in which the two algorithms work complementarily. More specifically, most ionosphere anomalies are detected by the first algorithm, while its undetectable conditions, which are quite rare but theoretically possible, are mitigated by the second. To evaluate the practical benefit of the monitor, we formulate a theoretical Vertical Protection Level (VPL), a conservative navigation error bound to guarantee the integrity requirement, for the monitor and conduct availability simulations using this VPL. These simulations show that the system with the monitor requires a smaller Vertical Alert Limit (VAL) to achieve the same availability as conventional single-frequency LAAS [10]. It is also shown that the level of improvement depends highly on the level of noise affecting the second algorithm.

2. REVIEW OF HYBRID DUAL-FREQUENCY LAAS

Hybrid dual-frequency LAAS uses DFree as its primary smoothing filter and switches to IFree when the ionosphere state is extremely anomalous. The main difference between DFree and IFree is the degree to which ionosphere effects are removed from the measurements. DFree partially removes the effects of ionosphere delays, while IFree completely removes the effects. Because of the immunity it offers against ionosphere-related errors, IFree appears on the surface to be a better method than DFree; however, its critical drawback is the large error size. Our previous study showed that this error is so big that IFree cannot achieve acceptable availability. Therefore, DFree should be used unless the ionosphere condition is discovered to be extremely anomalous [3].

To switch from DFree to IFree appropriately, the system needs an ionosphere monitor. Moreover, because DFree does not remove all ionosphere effects, it cannot guarantee the integrity against ionosphere fault without a monitor. In order to understand what quantities should be monitored, this section briefly reviews the theory of DFree and highlights the key equations describing ionosphere effects. We start with conventional single-frequency carrier-smoothing and proceed to DFree so that it can be seen how DFree reduces the effect of ionosphere-related errors. Detailed explanations of DFree can be found in [3,4,5].

Single-frequency carrier smoothing and DFree have the same filter structure, as shown in Figure 1. Here, Ψ represents the input signal containing code measurements, Φ represents the input signal containing carrier measurements, and τ (in the transfer function of the low-pass filter) is a smoothing time constant conventionally set to 100 seconds. The two filters are constructed so that the basic structure is maintained while the input signals are varied.

The single-frequency carrier-smoothing filter uses the L1 code measurement, ρ_1, for Ψ and the L1 carrier measurement, ϕ_1, for Φ. They are expressed as follows.

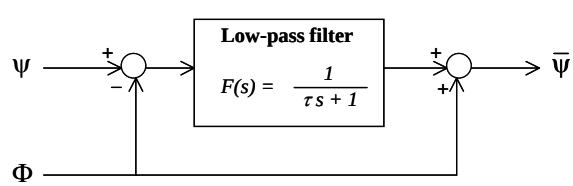

Figure 1: Block diagram of smoothing filter

$$\begin{aligned}\Psi &= \rho_1 = r + I_1 + \eta_1 \\ \Phi &= \phi_1 = r - I_1 + N_1\end{aligned} \tag{1}$$

Here, r includes all common terms between code and carrier such as range to the satellite, clock offsets, and the troposphere delay. I_1 represents the ionosphere delay, η_1 is the random noise on code measurements (e.g., thermal noise and multipath), and N_1 is the integer ambiguity of the carrier measurements. Random noise on carrier measurements is ignored, since it is much smaller than that on code measurements. The subscript "1" indicates that the measurements are on the L1 frequency.

Feeding these inputs into the filter shown in Figure 1, we obtain the following output, expressed in terms of its Laplace transform.

$$\overline{\Psi} = r + (2F - 1)I_1 + F\eta_1 \tag{2}$$

Here, F is the transfer function of the low-pass filter. The second term on the right-hand side of (2) describes the filtered ionosphere delays, and the third term represents the filtered random noise. Here, we are interested in the second term—the ionosphere term.

If the ionosphere delay in the input signal is constant, the low-pass filter does nothing to it (i.e., $(2F-1)I_1 = I_1$). However, if it varies with time, a "delay" effect is induced in the filter. To observe it, let us examine a case where the ionosphere delay has a constant temporal gradient, I_d.

$$I_1(t) = I_d t + I_0 \tag{3}$$

When the ionosphere effect on the raw-code measurements has this form, the filtered ionosphere impact, the second term in equation (2), becomes the following.

$$\text{Filtered Ionosphere}: \; I_1 - 2\tau I_d \tag{4}$$

This is the key equation for understanding the effect of the anomalous ionosphere on single-frequency LAAS. LAAS assumes that the filtered ionosphere is almost identical between the LGF and users. However, if there is a large spatial gradient in the ionosphere, meaning I_1 in equation (4) is significantly different between the LGF and users, it might cause a hazardously large error in user position estimation. Moreover, equation (4) shows that if the temporal ionosphere variation, I_d, is different between the LGF and users, it will cause an additional error in the position estimation.

In contrast, DFree eliminates the effect of temporal gradients due to ionosphere anomalies. It uses L1 code measurements and L1/L2 carrier measurements as inputs to the filter. These inputs are expressed as follows.

$$\begin{aligned}\Psi &= \rho_1 = r + I_1 + \eta_1 \\ \Phi &= \phi_1 - \frac{2}{\alpha}(\phi_1 - \phi_2) \\ &= r + I_1 + N_1 - \frac{2}{\alpha}(N_1 - N_2) + \frac{2}{\alpha}(IFB + \tau_{gd}) \\ \alpha &= 1 - f_{L1}^2 / f_{L2}^2\end{aligned} \tag{5}$$

Here, IFB is the interfrequency bias of the receiver which is caused by hardware differences between L1 and L2 signal paths, τ_{gd} is the interfrequency bias of the satellite transmitter which is also caused by the L1/L2 hardware differences [8,9], and f_{L1} and f_{L2} are the L1 and L2 frequencies (1575.42 and 1227.6 MHz, respectively).

Feeding these signals into the filter, we obtain the following output, again expressed in the Laplace domain.

$$\overline{\Psi} = r + I_1 + F\eta_1 \tag{6}$$

Note that the second term in (6) does not depend on the filter F, and hence the output does not suffer from the $2\tau I_d$ delay effect of (4) when exposed to a ramp ionosphere input. Moreover, the random noise on the output is identical in DFree and single-frequency carrier smoothing (compare the third term in equations (2) and (6)). By eliminating the effect of ionosphere divergence while keeping the noise level the same, DFree significantly improves the robustness of LAAS against ionosphere anomalies. On the other hand, because the raw-code ionosphere delay, I_1, remains in the output, large spatial gradients are still a potential threat for DFree.

Having specified the ionosphere error model for DFree, the quantity to be monitored has been made clear. We do not need to care about the temporal gradient errors that affect single frequency LAAS; however, we do care about the absolute delay differences because the accuracy of DFree still depends on them. Therefore, the monitor must observe absolute ionosphere differences between LGF and users.

3. OUTLINE AND ASSUMPTIONS OF THE MONITORING METHOD

Before starting the discussion of the monitor algorithms, it is important to clarify the assumptions we make in this paper. First, we assume the landing operation illustrated in Figure 2. In this configuration, the "landing threshold" or "decision point" is 5 km from the ground receiver and the user (an aircraft on final approach to the LGF-equipped airport) passes this point with the velocity of 0.07 km/s.

We also assume that anomalous ionosphere fronts are described by an ionosphere threat space model with three

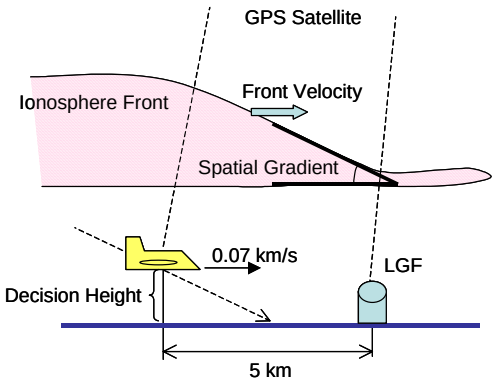

Figure 2: Illustration of landing operation with an ionosphere front present

parameters: gradient, velocity with respect to the ground, and width. This model is the same type as the recently-finalized "ionosphere anomaly threat model" for LAAS CAT I approaches [10]; however, since we are considering CAT III approaches, we allow for extra margin in the gradient magnitude as compared to the CAT I model. Table 1 shows the parameter ranges for this model.

Furthermore, we assume that both the LGF and users have an ionosphere monitor. This architecture is different from that of conventional single-frequency LAAS in which only the LGF has a monitor. Figure 3 shows an overview of the monitoring method. As the figure shows, two algorithms operate together: an algorithm based on temporal gradient estimation (discussed in Section 4), and an algorithm based on ionosphere delay estimation (discussed in Section 5). Each algorithm has its own test statistic and threshold; satellites whose test statistic exceeds the threshold are not used for navigation. After this threshold check, the airborne subsystem computes the Vertical Protection Level (VPL) for the remaining satellites (discussed in Section 6) and compares it with the Vertical Alert Limit (VAL) to decide whether or not to complete the landing.

Table 1: Parameter ranges of ionosphere threat space

Parameter	Range	Note
Gradient	35 ~ 400 (mm/km)	for all elevations
Velocity (V_{front})	0 ~ 0.75 (km/s)	--
Width	25 ~ 100 (km)	--

4. MONITOR ALGORITHM BASED ON TEMPORAL GRADIENTS

In Section 2, we noted that we do not need to observe temporal ionosphere gradients because the resulting divergence is not a threat to DFree. However, temporal gradients include useful information for detecting anomalous ionosphere behavior. Furthermore, they are relatively easy to observe and many monitors to detect anomalous temporal gradients have been previously introduced for use with CAT I LAAS (for example, see [6,7,11]).

This section discusses an algorithm that detects satellites exposed to anomalous ionosphere fronts by estimating temporal gradients. In the algorithm, the LGF and users independently detect satellites affected by anomalous ionosphere fronts, and the LGF broadcasts the results of its screening process to the user. Based on the identification of faulted satellites through a combination of airborne and ground monitoring, the user can estimate its position excluding the faulted satellites. We call this algorithm the "Rate-based algorithm".

4.1 Estimation of Ionosphere Temporal Gradients and Specification of the Threshold

The Rate-based algorithm estimates ionosphere temporal gradients using L1 and L2 carrier-phase measurements. First, the algorithm estimates the ionosphere delays using these measurements.

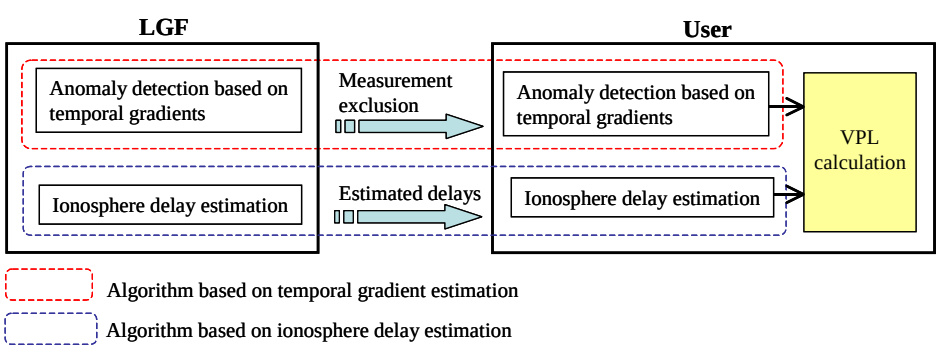

Figure 3: Monitor overview

$$\tilde{I}[k] = \frac{1}{\alpha}(\phi_2[k] - \phi_1[k])$$
$$= I[k] + \frac{1}{\alpha}(N_{12}[k] + IFB + \tau_{gd}) + \frac{1}{\alpha}\varepsilon_{12}[k] \quad (7)$$
$$(N_{12} = N_2 - N_1 \,,\, \varepsilon_{12} = \varepsilon_2 - \varepsilon_1)$$

Here, ε is the noise on the carrier measurements. Assuming no cycle slips are detected, instantaneous rates of change of these delays are computed as follows.

$$\tilde{\dot{I}}_{raw}[k] = \frac{1}{qT_{id}}(\tilde{I}[k] - \tilde{I}[k-q]) = \dot{I}[k] + \dot{\varepsilon}_{12}[k] \quad (8)$$

Here, T_{id} is the sampling period of the carrier measurements, which is set to 0.5 seconds, and q is an arbitrary integer that is set to 2 (by setting it to 2, we look 1 second backward in time). The raw rates from (8) are then fed into a low-pass filter to reduce the noise.

$$\hat{\dot{I}}[k] = \frac{\tau_{id} - 1}{\tau_{id}}\hat{\dot{I}}[k-1] + \frac{1}{\tau_{id}}\tilde{\dot{I}}_{raw}[k] \quad (9)$$

Here, τ_{id} is the time constant for the low-pass filter, herein set to 20 seconds.

The estimated gradient from (9), $\hat{\dot{I}}$, is then compared with a threshold to detect satellites affected by the anomalous ionosphere. A proper threshold is necessary to detect the faulted satellites correctly. We specify the threshold by applying the Gaussian overbound method described in [6,7] to the empirical data collected on April 12, May 19, and July 27, 2006. The distribution of the empirical gradients estimated by equations (7-9) of the above algorithm is shown in Figure 4, where the number of data points is about 4.5 million. This figure clearly shows that the gradient magnitudes depend on satellite elevation angles. We calculate the sample means and the sample standard deviations of the gradients in nine elevation bins of 10 degrees each. The discrete means and standard deviations are interpolated with a fourth-order polynomial, and continuous functions for the mean and standard deviation are obtained. The red and blue curves in Figure 4 show these functions. By normalizing the empirical gradients with these functions, gradients independent of elevation angles are obtained.

Figure 5 shows the cumulative distribution function (CDF) of the normalized gradients. Ideally, after normalization, these data should be distributed according to a Gaussian distribution with a standard deviation of 1. This ideal case is drawn as the red line in Figure 5. The plot shows that this Gaussian does not overbound the tails of the empirical data. With a parameter search, we find that if the standard deviation of the Gaussian is inflated by a factor of 1.56, the inflated Gaussian overbounds the normalized gradients. The green line in Figure 5 shows the inflated Gaussian. Applying the inflation factor to the original function of the sample standard deviations, we obtain a modified function which overbound the empirical data. The red curve in Figure 6 shows the inflated function, while the blue curve shows the original standard deviation.

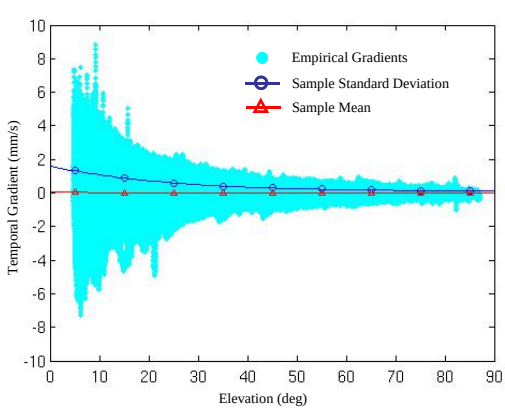

Figure 4: Distribution of empirical gradients

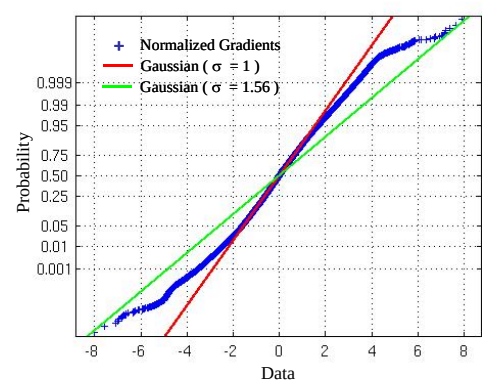

Figure 5: CDF of normalized gradients

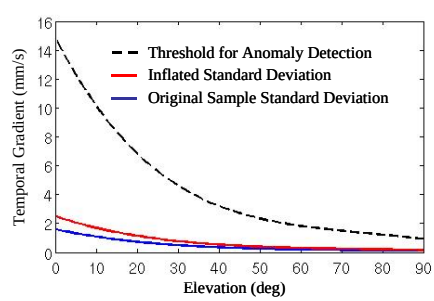

Figure 6: Threshold for anomaly detection

Finally, the elevation-dependent threshold is:

$$Th_{ig}(el) = \pm K_{ffd\_ig} 1.56\sigma_{ig}(el) \quad , \qquad (10)$$
$$K_{ffd\_ig} = 6$$

where σ_{ig} corresponds to the sample standard deviation as a function of elevation angle (the blue curve in Figure 6). The resulting threshold is shown in Figure 6 as a dashed curve. To obtain this threshold, the multiplier K_{ffd_ig} is set to 6 so that the theoretical probability of a fault-free alarm is less than 1.98×10^{-9}, which is considered sufficient for the continuity requirement for CAT III LAAS [12]. Distribution biases are small enough that they can be neglected (see the red curve in Figure 4).

It is also important to evaluate the response speed of the algorithm, a speed governed by the response of the low-pass filter given by equation (9). Figure 7 plots the step response of this filter, and it shows that the 90% settling time is about 23 seconds. Such a fast response can be achieved because only carrier measurements are used in the algorithm. The noise on carrier measurements is small to begin with and is further reduced by the 20-second time constant of the filter.

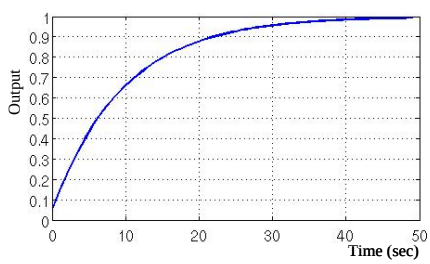

Figure 7: Step response of low-pass filter

4.2 Mapping Model from Temporal to Spatial Gradients

In order to analyze the performance of the Rate-based algorithm, it is necessary to convert the delay rate observation into an equivalent spatial gradient. For the mapping, we use a conventional model which assumes that a temporal gradient results from motion of an ionosphere-pierce-point (IPP) through an ionosphere front. Figure 8 is a schematic of this model. In this figure, an ionosphere front with a gradient of α mm/km is moving with a velocity of V_{front} km/s. The IPP is moving with a velocity of V_{IPP} km/s within the front. An angle θ exists between the front movement and IPP movement directions. In this case, the ionosphere delay varies with the following rate of change.

$$\dot{I} = \alpha(V_{IPP}\cos\theta - V_{front})$$

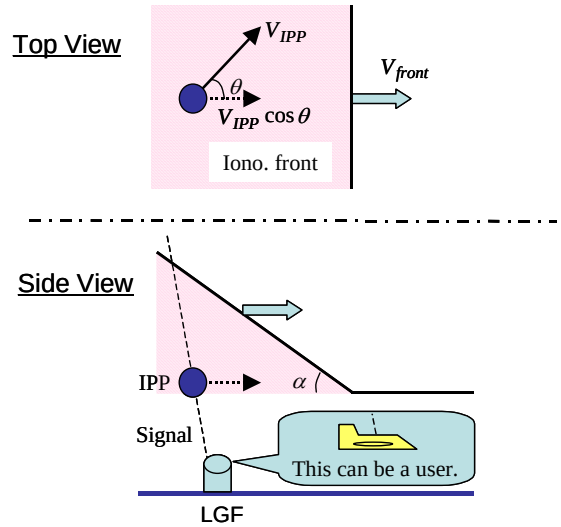

Figure 8: Schematic expression of model that transforms temporal gradients into spatial gradients

Rearranging and generalizing this equation, we obtain the following model connecting temporal and spatial gradients.

$$spatial\ gradient\ (\text{mm/km}) = \frac{temporal\ gradient\ (\text{mm/s})}{dV_{front/IPP}\ (\text{km/s})} \qquad (11)$$
$$dV_{front/IPP} = V_{IPP}\cos\theta - V_{front}$$

Here, $dV_{front/IPP}$ is the ionosphere front velocity with respect to the (moving) IPP.

Using this model, the threshold of the temporal gradient shown in Figure 6 can be transformed into a spatial-gradient threshold. Figure 9 shows this threshold as a function of $dV_{front/IPP}$ given an elevation angle. The maximum gradient of 400 mm/km in these plots comes from the upper bound in the assumed threat space (see Table 1). The upper-right area of each curve corresponds to detectable ionosphere fronts, and the lower-left area corresponds to undetectable fronts. Figure 10 shows a different view of

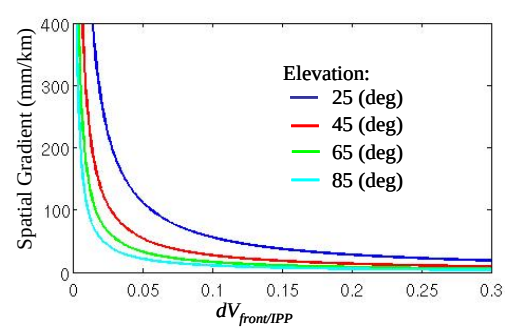

Figure 9: Threshold of spatial gradients as a function of $dV_{front/IPP}$

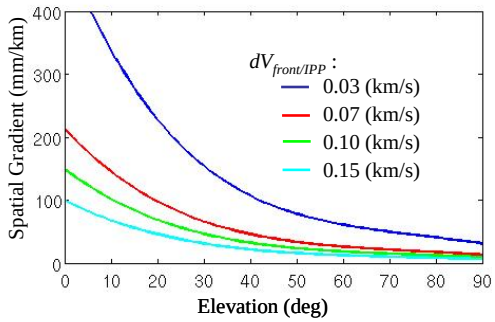

Figure 10: Threshold of spatial gradients as a function of elevation angle

this threshold, where the threshold is drawn as a function of elevation angles given a particular $dV_{front/IPP}$. As in Figure 9, the upper-right area of each curve corresponds to detectable fronts.

4.3 Undetectable Ionosphere Fronts and the Worst-Case Scenario

As Figure 9 and 10 show, certain ionosphere fronts with a large gradient lie below the threshold. In particular, the smaller $dV_{front/IPP}$ becomes, the larger the gradients of fronts lying below the threshold are. The fronts below the threshold are unlikely to be detected by the Rate-based algorithm; hence, the "amount" of undetectability depends on $dV_{front/IPP}$.

Although certain ionosphere fronts are undetectable to the Rate-based algorithm, the algorithm can nevertheless serve a role by limiting the number of satellites simultaneously affected by the fronts. The remainder of this section justifies this limit to be two satellites. Because we are interested in the most severe condition for the algorithm, an ionosphere front with the maximum gradient allowed by the threat model (400 mm/km) is considered. The symbol $IPP_{i,u}$ is used in this discussion to designate the IPP between satellite *i* and the user (for LGF, $IPP_{i,g}$ is used).

The analysis begins with the cases where the front affects a single satellite. If the front almost synchronizes with $IPP_{i,u}$ (namely $dV_{front/IPP}$ for the user is close to zero), the airborne monitor cannot detect the front. If in this case the associated IPP for the LGF ($IPP_{i,g}$) does not fall within the expanse of the ionosphere front, as shown in Figure 11(a), then a hazardous situation occurs. By contrast, the LGF monitor will almost certainly detect the front if the IPP for the LGF does fall within the expanse of the ionosphere front, as shown in Figure 11(b). This is because the IPP for the LGF has a relative velocity of 0.07 km/s against the front (recall that the user has 0.07 km/s velocity at the decision point) and the algorithm detects the front with the maximum gradient for $dV_{front/IPP}$ of about 0.07 km/s

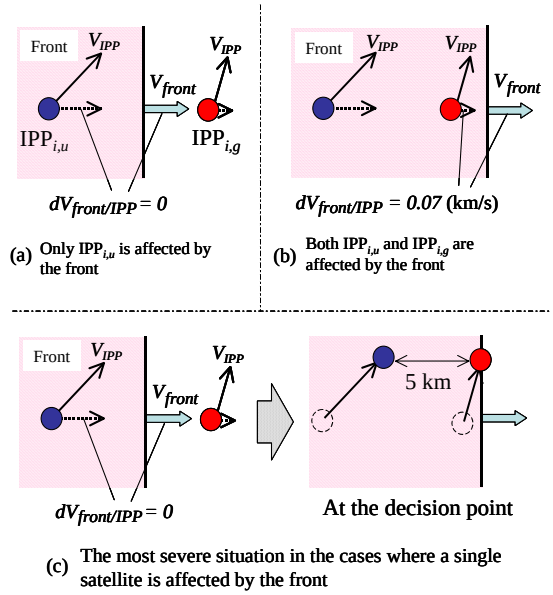

Figure 11: Geometrical explanations for cases where an ionosphere front affects a satellite

(confirm that 400 mm/km is above the red curve in Figure 10). Based on this geometrical analysis, it can be said that when the front moves with the IPP of the user and hits the LGF IPP just as the user passes the decision point, as shown in Figure 11(c), both the airborne and ground monitor cannot detect the front, and hence this situation is the most severe condition for one-satellite-affected cases.

Next, we analyze the case where the front simultaneously affects two satellites, say, satellites *i* and *j*. There are four pierce points to be considered: $IPP_{i,u}$, $IPP_{i,g}$, $IPP_{j,u}$, and $IPP_{j,g}$. Although $IPP_{i,u}$ and $IPP_{j,u}$ have independent velocities, theoretically, there is a front which is synchronized with both IPPs and hence cannot be detected by the airborne monitor (Figure 12 illustrates such a front). In most circumstances, the ground monitor detects such a front. However, as shown in Figure 13, when the front motion direction is perpendicular to the baseline of $IPP_{i,u}$ and $IPP_{j,u}$, and the leading edge of the front is less than 5 km from the baseline, the ground monitor cannot detect the front either.

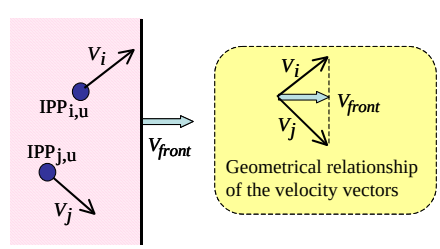

Figure 12: Geometrical explanation for a front moving synchronously with two IPPs

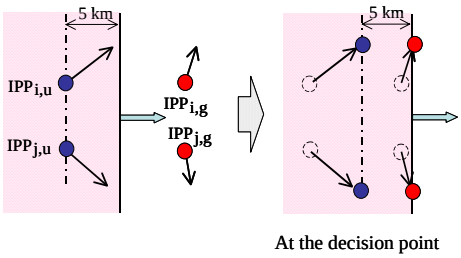

Figure 13: Most-severe condition for the two-satellite-affected case

This is because $IPP_{i,g}$ and $IPP_{j,g}$ do not "catch up to" the front before the user passes the decision point. If this particular situation occurs, the Rate-based algorithm cannot detect the front even though it affects two satellites simultaneously.

To confirm if such a special condition would occur in practice, we investigated actual satellite geometries for three airports (Memphis, Los Angeles, and New York). We searched for the geometry where the baseline of two IPPs was perpendicular to the direction of the undetectable front and found some IPP pairs that satisfied the condition (detailed explanations of this investigation can be found in [13]). These IPP pairs have potential to experience the condition where the Rate-based algorithm can miss detecting the fronts affecting these IPP pairs. Because of the existence of the potentially vulnerable geometries, and considering the very stringent integrity requirement for CAT III LAAS, we cannot neglect the threat of a front simultaneously affecting two satellites without being detected by the Rate-based algorithm.

Expanding the analysis above, we can also construct the theoretical condition where the Rate-based algorithm misses detection of fronts simultaneously affecting three satellites. In this condition, as shown in Figure 14, three IPPs align on a single line. The front is synchronized with all the three IPPs, and the leading edge of the front is less 5 km from the baseline of the IPPs. In the time before the user passes the decision point, neither the airborne monitor nor the ground monitor can detect the front satisfying this condition.

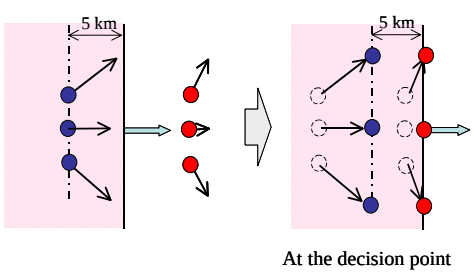

Figure 14: Most-severe condition for the three-satellite-affected case

To confirm if such a special condition would occur in practice, we again investigated the satellite geometries for the three airports mentioned above. We searched for a geometry where three IPPs align on a single line and there exists a velocity that synchronizes with all the three IPPs. This time, we did not find any IPP triplets which satisfied the condition. This result means that, at least for the three airports searched in depth, there are no geometries that experience the condition where the Rate-based algorithm can miss detecting fronts affecting three or more satellites.

These simulations do not constitute a formal integrity proof. However, considering the very improbable nature of these conditions, we conclude that, in practice, the Rate-based algorithm always detects an ionosphere front if it simultaneously affects three or more satellites, but that the algorithm may miss detecting fronts simultaneously affecting only two satellites.

As a footnote, in the above analysis, we considered only the cases where the front moved with IPPs for the user and hit the associated IPPs for the LGF just as the user passed the decision point. The same discussion is applicable to the cases where the front moves with IPPs for the LGF and hits the IPPs for the user when the user passes the decision point. This situation can also be critical for the Rate-based algorithm.

5. MONITOR ALGORITHM BASED ON IONOSPHERE DELAYS

Another approach to detect anomalous spatial gradients is to compare the ionosphere delays estimated by the LGF and users. There is no completely undetectable front in this approach. Moreover, the concept is feasible because the use of dual-frequency GPS enables us to directly estimate ionosphere delays. This algorithm is summarized as follows. First, the user and LGF independently estimate the ionosphere delays. Next, the LGF broadcasts its delays to the user. Finally, the user compares the two delays and monitors for the possible existence of an ionosphere front. We call this algorithm the "Delay-based algorithm".

5.1 Ionosphere Delay Estimation

Ionosphere delays can be estimated by using dual-frequency code/carrier measurements and carrier-smoothing filter shown in Figure 1 [4]. The input signals to the filter are given as follows.

$$\Psi = \frac{1}{\alpha}(\rho_1 - \rho_2) = I_1 + \frac{1}{\alpha}(\eta_1 - \eta_2) - \frac{1}{\alpha}(IFB + \tau_{gd})$$

$$\Phi = \frac{1}{\alpha}(\phi_2 - \phi_1) = I_1 + \frac{1}{\alpha}(N_2 - N_1) + \frac{1}{\alpha}(IFB + \tau_{gd})$$

Feeding these inputs into the filter, ionosphere delays are estimated using the following equation, expressed in the Laplace domain.

$$\begin{aligned}\overline{\Psi} &= \hat{I} \\ &= I + \frac{1}{\alpha}(F\eta_1 - F\eta_2) - \frac{1}{\alpha}(IFB + \tau_{gd})\end{aligned} \tag{12}$$

The algorithm faces two significant problems: large noise errors and interfrequency biases. First, we study in detail the noise—the second term in the second line of equation (12). Assuming that the L1/L2 raw code noise terms, η_1 and η_2, are white Gaussian, then the filtered noise, $F\eta_1$ and $F\eta_2$, can be modeled as the Gaussian noise whose standard deviations, σ_1 and σ_2, are given as follows [4,5].

$$\sigma_1 = \sigma_{\rho 1}\sqrt{T/2\tau} \quad , \quad \sigma_2 = \sigma_{\rho 2}\sqrt{T/2\tau} \tag{13}$$

Here, T is the sampling period of the code measurements, τ is the smoothing time constant of the filter, and $\sigma_{\rho 1}$ and $\sigma_{\rho 2}$ are the standard deviations of the L1/L2 raw code noise.

From equations (12) and (13), the standard deviation of the random noise on the ionosphere delay estimation, σ_{Ihat}, is given as the following, assuming that the filtered noise on L1/L2 frequencies, $F\eta_1$ and $F\eta_2$, are independent and that their standard deviations, σ_1 and σ_2, are identical.

$$\begin{aligned}&\sigma_{Ihat} = \sqrt{\frac{1}{\alpha^2}(\sigma_1^2 + \sigma_2^2)} = 2.19\sigma_1 \\ &(\alpha = 1 - f_{L1}^2 / f_{L2}^2 = -0.6469)\end{aligned} \tag{14}$$

Here, σ_1 is theoretically identical to the standard deviation of the errors on code measurements smoothed by single-frequency carrier-smoothing. Thus it is possible to leverage single-frequency error models to describe σ_1. Specifically, standard models exist to describe the single-frequency carrier-smoothing error for the case of a sampling period, T, and smoothing time constant, τ, of 0.5 seconds and 100 seconds respectively [14]. These models are called Airborne Accuracy Designators (AAD) for the airborne subsystem and Ground Accuracy Designator (GAD) for the ground subsystem. Equation (14) indicates that we can use them to construct an error model for ionosphere delay estimation. The blue curve in Figure 15 shows the model for the user's estimation errors (denoted as $\sigma_{Ihat,u}$) based on AAD-B, and the red curve shows the one for LGF's estimation errors (denoted as $\sigma_{Ihat,g}$) based on the GAD-C4 model ("C4" indicates that a 4-reference-receiver ground-system configuration is assumed).

5.2 Test Statistic and Threshold Specification

In this method, the LGF and the user independently

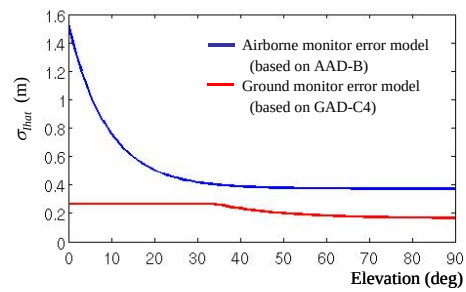

Figure 15: Ionosphere delay estimation error model

estimate ionosphere delays, and the LGF broadcasts its delay estimates to the user. Each user then computes the difference between the LGF's delay estimates and its own as follows.

$$\Delta\hat{I}_{ug}^i = \hat{I}_u^i - \hat{I}_g^i = \Delta I_{ug}^i + \frac{1}{\alpha}\Delta IFB_{ug} + \varepsilon_{ug}^i \tag{15}$$

Here, ΔI_{ug}^i represents the true differential range error caused by an ionosphere front affecting satellite i, and ε_{ug}^i is the random noise. Note that the interfrequency bias of the satellite, τ_{gd} in equation (12), is canceled out because it is a unique value for each satellite and thus affects the LGF and user equally.

Let us denote the standard deviation of ε_{ug}^i as $\sigma_{\Delta I}^i$. This term consists of the root-sum-square of random errors which independently affect the estimation of ΔI_{ug}^i.

$$\sigma_{\Delta I}^i = \sqrt{\sigma_{Ihat,u}^i + \sigma_{Ihat,g}^i + \sigma_{iono}^i} \tag{16}$$

Here, $\sigma_{Ihat,u}$ and $\sigma_{Ihat,g}$ are the estimation errors of ionosphere delays at the user and LGF, and σ_{iono} is the sigma of nominal ionosphere difference between the user and LGF which is given as follows.

$$\sigma_{iono}^i = d_{gu}\sigma_{vig}Oq^i$$

Here, d_{gu} is the distance between the user and LGF (set to 5 km, recall section 3), σ_{vig} is the nominal ionosphere spatial gradient in the zenith domain and is set to 5 mm/km, and Oq^i is the obliquity factor corresponding to the elevation of satellite i. Using AAD-B and GAD-C4 for the airborne and ground monitors (i.e., using the models shown in Figure 15), $\sigma_{\Delta I}$ is plotted in Figure 16.

Having modeled the random part of the $\Delta\hat{I}_{ug}^i$, we next need to deal with the bias part—ΔIFB in equation (15). To cancel out this value, we take a *double-difference* of $\Delta\hat{I}_{ug}^i$. Since Figure 16 shows that the estimation error decreases as

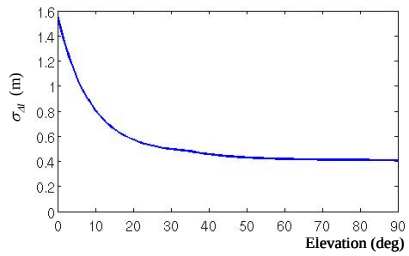

Figure 16: Test statistic error model

the elevation increases, the double-difference should be taken between the highest satellite and the other satellites so that the noise can be kept small. Supposing that there are N satellites in view and that the indexes of these satellites (i = 1,2,…,N) are assigned in the ascending order of elevation, the double-difference of $\Delta\hat{I}_{ug}^{i}$ is given as follows.

$$\nabla\Delta\hat{I}_{ug}^{i} = \Delta\hat{I}_{ug}^{i} - \Delta\hat{I}_{ug}^{N} = \Delta I_{ug}^{i} - \Delta I_{ug}^{N} + \varepsilon_{ug}^{iN} \quad (i = 1,\cdots,N-1) \tag{17}$$

This quantity is the test statistic to detect satellites affected by an ionosphere front. Because the differential range errors—ΔI_{ug}^{i} and ΔI_{ug}^{N} in equation (17)—are zero under the nominal ionosphere conditions (recall that nominal ionosphere error is included in the random part: equation (16)), the nominal distribution of the test statistic is assumed to be a zero-mean Gaussian whose standard deviation is given by:

$$\sigma_{\Delta I}^{i} = \sqrt{(\sigma_{\Delta I}^{i})^2 + (\sigma_{\Delta I}^{N})^2}\ , \tag{18}$$

where each sigma in the right-hand side of the equation is given by equation (16). Using this sigma, the threshold for the test statistic is given as follows.

$$Th_{\Delta I}^{i} = \pm K_{ffd\_\Delta I}\sigma_{\Delta I}^{i} \quad (i = 1,2,\cdots,N-1) \qquad K_{ffd\_\Delta I} = 6 \tag{19}$$

The allocation of 6 for $K_{ffd\_\Delta I}$ is based on the same reasoning used to compute the multiplier K_{ffd_ig} for the Rate-based algorithm (see Subsection 4.1).

It may be noticed that the test statistic and the threshold are defined only for satellite 1 to N–1. For the highest satellite (satellite N), there is no unique monitor statistic. As such we use the same value for satellite N as that for the second highest satellite (satellite N–1):

$$\nabla\Delta\hat{I}_{ug}^{N} = \nabla\Delta\hat{I}_{ug}^{N-1} \quad \text{and} \quad Th_{\Delta I}^{N} = Th_{\Delta I}^{N-1}. \tag{20}$$

The test statistic and the threshold for the highest satellite are not used in the detection of faulted satellites; however, they are needed in the computation of VPL (described in Subsection 6.3).

5.3 Detection Rule

The specific detection (and exclusion) rule is given as follows.

> <u>Detection Rule</u>: If the test statistic $\nabla\Delta\hat{I}^{i}$ exceeds the threshold $Th_{\Delta I}^{i}$, exclude satellite i and satellite N (the highest satellite).

Note that not only satellite i but also satellite N is excluded, because the differential range errors on both satellites can inflate the test statistic $\nabla\Delta\hat{I}^{i}$, and because it cannot be determined which error actually causes the anomalous statistic. Although this rule is somewhat conservative, the conservativeness will not be a drawback in practice. Because the Rate-based algorithm effectively excludes almost all satellites affected by ionosphere fronts, the Delay-based algorithm will mostly monitor "clean" satellites. Accordingly, the Delay-based algorithm has the responsibility of detecting faulted satellites only under the extremely rare geometry conditions described in Subsection 4.3.

5.4 Sensitivity of the Algorithm

It is important to discuss the sensitivity of the algorithm, because Figure 16 implies a large noise level for the test statistic. If the test statistic is noisy, the thresholds must be set loose, making detection difficult.

One way to lower the noise is to employ a long time constant for the filter that estimates ionosphere delays. Equation (13) indicates that the standard deviation of the output noise of the filter is in inverse proportion to the square-root of the time constant. Hence, theoretically, as the time constant increases by a factor of 4, the output noise decreases by a factor of 2, and so does the threshold. Figure 17 shows an example of thresholds corresponding to a particular geometry. Figure 17(a) shows three thresholds for each satellite whose position in sky is shown in Figure 17(b). The largest thresholds (blue circles) are obtained using AAD-B and GAD-C4 (with a 100-second time constant). The other two are obtained by setting the time constant to 500 seconds and to 1000 seconds.

Recall that the maximum error due to an ionosphere gradient is 2 m (400 mm/km times 5 km). Because the thresholds for the case of 100-second smoothing are so loose that they exceed the 2 m maximum error, the algorithm can be seen to be ineffective unless the time

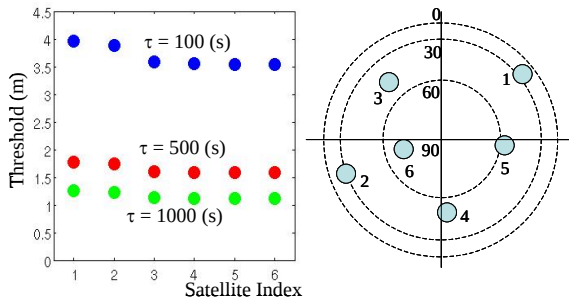

(a) Thresholds (b) Satellite Position

Figure 17: Thresholds for a particular geometry

constant parameter is increased. Availability simulations (Section 7) suggest that a time constant of 1000 seconds or longer is desired for practical applications.

6. VPL DERIVATION FOR THE IONOSPHERE MONITOR

We have introduced two algorithms to detect satellites affected by anomalous ionosphere fronts. This section derives a Vertical Protection Level (VPL) which is customized to the algorithms. First, we derive a general form of the VPL by discussing the relationship between the VPL and the integrity risk corresponding to ionosphere anomalies. Next, we derive two VPLs based on two systems: one has only the Rate-based algorithm, the other has both monitor algorithms. The first system is considered as a baseline because it requires no change to the message structure broadcasted by the LGF [12]. The second is an enhanced system because we can anticipate performance improvement from the baseline system due to the Delay-based algorithm, even though it requires an additional message broadcasting—the estimated ionosphere delays.

6.1 Definition of VPL_{iono} and Relationship between VPL_{iono} and Integrity Risk

In order to determine the VPL, we consider the worst case mode in which an ionosphere front harms user's position estimation. Because the Rate-based algorithm is considered to detect all ionosphere fronts affecting three or more satellites, the fault mode can be reduced to the following.

> Fault mode: A situation where an ionosphere spatial gradient simultaneously affects at most two satellites without being detected by the Rate-based algorithm.

The vertical navigation error, E_{iono}, under the fault mode is expressed as the sum of the random error associated with the nominal ranging measurements and the bias induced by the undetected ionosphere front.

$$E_{iono} = E_{random} + Bias(\Delta I^i, \Delta I^j) \qquad (21)$$

Here, ΔI^i and ΔI^j represent the differential range errors of satellite i and j caused by the ionosphere front, and $Bias(\Delta I^i, \Delta I^j)$ is the bias induced by these errors. The random error E_{random} has a zero-mean Gaussian distribution whose standard deviation, σ_v, is assumed to be:

$$\sigma_v = \sqrt{\sum_{k=1}^{N} S_{v,k}^2 \sigma_k^2} \ .$$

Here, σ_k is the nominal range error for satellite k which includes ground receiver's noise, airborne receiver's noise, and errors caused by the nominal ionosphere gradient. The terms $S_{v,k}$ are the relevant coefficients from the weighted pseudoinverse range-to-position transformation matrix **S**. The probability distribution for the positioning error, E_{iono}, is thus given as:

$$p(E_{iono}) \sim \mathcal{N}(Bias(\Delta I^i, \Delta I^j), \sigma_v) \ . \qquad (22)$$

Considering this positioning error, the VPL accounting for the ionosphere fault (denoted as VPL_{iono}) is defined as follows.

> VPL_{iono}: A protection level determined such that the total probability of occurrence for a vertical positioning error (induced by an ionosphere front) beyond the level does not exceed the integrity risk allocated for the fault mode.

Because there is no authorized allocation of the allowable integrity risk for the ionosphere fault, we tentatively allot 10^{-10} to the integrity risk—10% of the total integrity requirement for CAT III approaches (10^{-9}) [12]. The remainder of this section will derive quantitative expression for the VPL_{iono}.

The risk due to an ionosphere fault involves three events: first, an ionosphere anomaly occurs; second, the ionosphere monitor fails to detect the anomaly; and finally, VPL_{iono} fails to bound the fault-induced error given that the monitor has failed. Each of these events has a probability: P_{iono}, the prior probability of ionosphere anomalies; P_{md}, the conditional probability of missed-detection by the ionosphere monitor given the existence of the anomaly; and P_{pl}, the conditional probability that the error exceeds the protection level given the missed-detection. To meet integrity, the product of these probabilities must not exceed the integrity risk allotment, P_a (as noted above, 10^{-10} is allocated to this P_a).

$$P_a \geq P_{pl} P_{md} P_{iono} \ .$$

Because there is no "provable" prior probability of ionosphere anomalies, we conservatively set P_{iono} to 1. Accordingly, the maximum allowable risk that the error exceeds the protection level given the missed-detection is expressed as:

$$P_{pl}^{*} = \frac{P_a}{P_{md}} . \qquad (23)$$

The value of the protection level is set so that the risk of an exceedance does not surpass the maximum risk given by the above equation. Accordingly, the probability of the vertical positioning error, described by (21), is integrated up to P_{pl}^{*} to determine the protection level. Figure 18 schematically expresses this derivation of the VPL from P_{pl}^{*}. The bell-shape curve in the figure shows the probability distribution of the positioning error given an ionosphere fault which the monitoring algorithms have failed to detect. The gray region in the figure corresponds to the probability that the error exceeds the protection level given the missed-detection, which is approximately equal to P_{pl}^{*}. The VPL_{iono} is hence mathematically expressed as follows.

$$VPL_{iono} = -Q^{-1}(P_{pl}^{*})\sigma_v + Bias(\Delta I^i, \Delta I^j) . \qquad (24)$$

In the following sections, we customize this VPL_{iono} equation for the two systems of interest (the baseline and enhanced systems), determining the random term ($-Q^{-1}(P_{pl}^{*})\sigma_v$) and bias term ($Bias(\Delta I^i, \Delta I^j)$) of equation (24) on a system-specific basis.

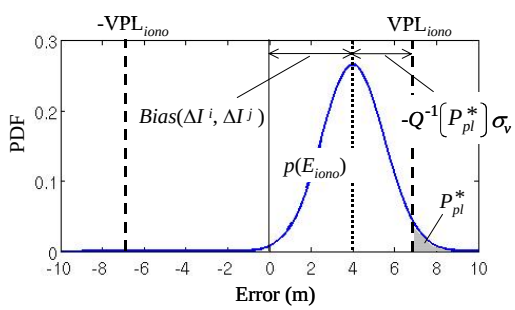

Figure 18: Distribution of positioning error and VPL_{iono}

6.2 VPL_{iono} for the Baseline System

This section derives VPL_{iono} customized to the baseline system in which only the Rate-based algorithm operates. The worst-case unobservable geometry for the Rate-based algorithm governs performance of this system. Specifically, to cover the unobservable conditions, P_{md} is set to 1. By setting the probability of missed-detection to 1, it appears that the Rate-based algorithm does not contribute to mitigation of the ionosphere risk. However, the monitor has already contributed by reducing the set of ionosphere threats to cases in which no more than two satellites are simultaneously affected by an ionosphere front. Setting P_{md} to 1, P_{pl}^{*} becomes equal to P_a which was set to 10^{-10} (see equation (23)). Consequently, the random part of VPL_{iono} becomes $6.3613\sigma_v$.

The bias part of VPL_{iono} should be the maximum bias in the fault mode. Because we are considering ionosphere fronts affecting at most two satellites, the maximum bias occurs when a front of the maximum gradient hits the most sensitive satellite or satellite pair in the current geometry. This maximum bias is expressed as:

$$Bias_{\max} = \max\left(\max_{i}\left(\left|S_{v,i}\right| \Delta I_{\max} \right), \max_{i,j}\left(\left|S_{v,i} + S_{v,j}\right| \Delta I_{\max} \right) \right), \qquad (25)$$

where ΔI_{max} is the maximum differential range error induced by the front, which in this paper is set to 2 m (the maximum gradient of 400 mm/km times the user-to-LGF separation of 5 km). In most cases, the maximum error of the two-satellite-affected situation, the second argument of the outer max(•), is larger than that of one-satellite-affected situation, the first argument. Taking the maximum between them takes account of geometries like the one whose S_v is, for example, given as S_v = [-2.12, 0.67, 0.54, 0.03, 0.88]. In this example, the maximum bias for the two-satellite-affected situation is 4.18 m, while that for the one-satellite-affected situation is 4.24 m.

Combining the random and bias parts, VPL_{iono} for the baseline system is given as:

$$VPL_{iono} = 6.3613\sigma_v + Bias_{\max} . \qquad (26)$$

Because σ_v and $Bias_{\max}$ depends only on the satellite geometry, users can easily compute VPL_{iono} at each epoch for the baseline system.

6.3 VPL_{iono} for the Enhanced System

This section specifies the random and bias parts of equation (24), to tailor the VPL_{iono} equation for the enhanced system which executes both the Rate-based and Delay-based algorithms. Recall that VPL_{iono} is computed after the monitoring algorithms have screened out satellites faulted by ionosphere fronts. Because the probability of missed-detection relates the fault observability to VPL_{iono}, the P_{md} plays an important role in the derivation of VPL_{iono}.

Let us write again equation (17) and (20)—the test statistic of the Delay-based algorithm.

$$\begin{aligned} \nabla\Delta\hat{I}^{i} &= \Delta I^{i} - \Delta I^{N} + \varepsilon^{iN} \quad (i = 1,\ldots,N-1) \\ \nabla\Delta\hat{I}^{N} &= \nabla\Delta\hat{I}^{N-1} \end{aligned} \tag{27}$$

The probability distribution of the test statistic given a hypothetical differential range error on the i-th satellite, ΔI^i, is mathematically expressed as follows.

$$p(\nabla\Delta\hat{I}^{i}) \sim \mathcal{N}(\Delta I^{i} - \Delta I^{N}, \sigma_{\Delta I}^{i}) \tag{28}$$

The standard deviation of the test statistic is given by equation (18), and ΔI^i (i = 1,…, N) varies from 0 m to 2 m. A missed detection event occurs when the test statistic fails to exceed the threshold given during a fault event. The P_{md} is thus the integral of distribution (28) for all values between the positive and negative thresholds. This integrated probability, illustrated as the gray region of Figure 19, is described by the following equation.

$$P_{md}(\Delta I^{i}) = Q\left(\frac{Th_{\Delta I}^{i} - (\Delta I^{i} - \Delta I^{N})}{\sigma_{\Delta I}^{i}}\right) - Q\left(\frac{-Th_{\Delta I}^{i} - (\Delta I^{i} - \Delta I^{N})}{\sigma_{\Delta I}^{i}}\right) \tag{29}$$

Here, the threshold is given by equation 19. Because the Rate-based algorithm ensures that ionosphere fronts affect at most two satellites, hypothetical range errors for at most two satellites, ΔI^i and ΔI^j, need to be considered. A conservative expression for the probability that the Delay-based algorithm misses detecting the hypothetical front is expressed as:

$$P_{md}(\Delta I^{i}, \Delta I^{j}) = \min(P_{md}(\Delta I^{i}), P_{md}(\Delta I^{j})). \tag{30}$$

Taking the minimum of $P_{md}(\Delta I^i)$ and $P_{md}(\Delta I^j)$ is justified, because it takes credit for only one of the available test statistics (the best one). If in fact the test statistics were independent, then we could take credit for the joint P_{md} being the product of the independent statistics. Because the differential errors are correlated (they are caused by the same ionosphere front), it is safest to use the upper bound (equation (30)). Equations (29) and (30) indicate that the

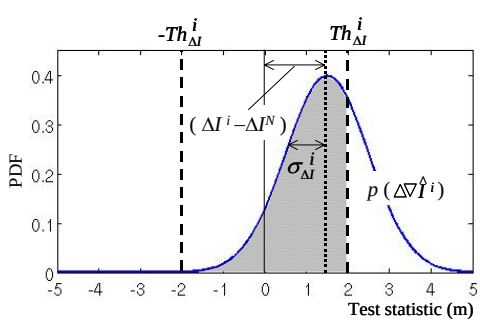

Figure 19: Probability of missed-detection (shaded gray)

probability of missed-detection decreases as the hypothetical differential range errors increase.

Note that, when one of the two satellites is the highest satellite, $P_{md}(\Delta I^N)$ is computed by using the test statistic and the threshold for the second highest satellite (recall equation (20)). Here, we need a caveat when the two satellites are the highest and the second highest satellites. First, the test statistics and the thresholds of these satellites are identical; hence, comparing the P_{md} of these satellites in equation (30) does not make sense for this case. More seriously, non-zero range errors on these satellites (ΔI^N and ΔI^{N-1}) cancel out in the computation of the test statistic (see equation (27)). Because of the cancellation, the probability of missed-detection could be inflated even for the large range errors. This unpleasant situation can be avoided by introducing a P_{md} of another satellite. Because the highest satellite is excluded whenever a test statistic of another satellite exceeds its threshold (recall the detection rule discussed in Subsection 5.3), P_{md} for any satellites in view can be used to evaluate the P_{md} for the highest satellite. Considering that the threshold of the third highest satellite (satellite N-2) is tightest in the other satellites, P_{md} for the front affecting the highest and the second highest satellites is given as follows.

$$P_{md}(\Delta I^{N}, \Delta I^{N-1}) = \min(P_{md}(\Delta I^{N-1}), P_{md}(\Delta I^{N-2})) \tag{31}$$

Substituting P_{md} computed by equation (30) or (31) for the random part of equation (24) and explicitly evaluating the bias part of the equation, the VPL corresponding to a particular satellite pair (i and j) and particular differential-range-errors on these satellites (ΔI^i and ΔI^j) is given as follows.

$$VPL_{i,j}(\Delta I^{i}, \Delta I^{j}) = -Q\left(\frac{P_a}{P_{md}(\Delta I^{i}, \Delta I^{j})}\right)\sigma_v + \left|S_{v,i}\Delta I^{i} + S_{v,j}\Delta I^{j}\right| \tag{32}$$

VPL_{iono} for the current geometry is the maximum of the $VPL_{iono}(\Delta I^i, \Delta I^j)$ in all possible satellite pairs and all possible differential-range-error pairs.

$$VPL_{iono} = \max_{i,j}\left(\max_{\Delta I^{i}, \Delta I^{j}}\left(VPL_{i,j}(\Delta I^{i}, \Delta I^{j})\right)\right) \tag{33}$$

Compared with VPL_{iono} of the baseline system, computation cost is a drawback of VPL_{iono} for the enhanced system. In equation (33), the airborne subsystem has to search for a maximum across many satellite pairs and many differential error pairs at each epoch, while VPL_{iono} for the baseline system is explicitly given by equation (26). However, VPL_{iono} for the enhanced system is theoretically smaller than the other: the random part is smaller than that of the baseline system because P_{md} is less than one, and the bias

part is obviously no more than the $Bias_{\max}$ of the baseline system. Therefore, we anticipate that the enhanced system will achieve higher availability than the baseline system does.

7. AVAILABILITY SIMULATIONS

In order to evaluate the effect of the monitoring algorithms, we conducted availability simulations for the two systems: the baseline system, and the enhanced system. Assuming these two system configurations, we estimated the availability for three airports: Memphis, Los Angeles, and New York.

System availability was computed as the average of "instantaneous" availability for all possible satellite geometries [3,15]. The almanac of 24-satellite constellation on July 1, 1993 was used to generate the geometries [16]. We simulated not only the situations where all satellites were healthy but also those where multiple satellites were unhealthy, using the "historical" probability of satellite malfunction [3,15].

As discussed in Subsection 5.4, the sensitivity of the Delay-based algorithm depends on the time constant of the delay-estimation filter. Specifically, the threshold to detect faulted satellites is tightened with longer time constants. To evaluate the practical benefit of the long time constant, we computed the availability of the enhanced system using three time constants: 100 seconds, 500 seconds, and 1000 seconds.

Table 2 shows the availability assuming 10-meter VAL. As shown in the table, the enhanced system with 100-second time constant achieves the same availability as the baseline system for all the airports. In other words, the Delay-based algorithm offers no benefit when the time constant is 100 seconds. This must be due to the very large noise of the ionosphere delay estimation in the algorithm, noise results in loose thresholds relative to the differential range errors (recall Figure 17). Consequently, without a long time constant, the probability of missed detection becomes large. Obviously, with a large probability of missed-detection, the effect of the algorithm is limited. According to the simulation result, a time constant of 1000 seconds or longer would be necessary to obtain conspicuous effect from the Delay-based algorithm.

Table 2: Availability (%) for 10 m VAL

		Memphis	LA	NY
Baseline		96.515	98.938	99.983
Enhanced	τ : 100 s	96.515	98.938	99.983
	τ : 500 s	96.518	99.286	99.984
	τ : 1000 s	97.903	99.982	99.987

Next, we searched for VALs for which the baseline system and enhanced system (with a 1000-second time-constant) can achieve 99.9% and 99.999% availabilities. Here, the 99.999% availability is desired for CAT III LAAS [12]. Table 3 gives the results. As a reference, a prior study [10] showed that, under a less severe ionosphere condition than that of our simulations, conventional single-frequency LAAS would require a VAL over 20 m to achieve 99.9% availability in Memphis. Compared with this estimation, both of baseline and enhanced systems need much smaller VAL (16.5 m and 14.5 m) to obtain the same availability in Memphis.

The performance improvement by the baseline system can be explained by two reasons. One is the use of DFree that significantly reduces the differential range errors caused by ionosphere fronts, eliminating the effect of the ionosphere temporal gradients ($2\tau I_d$ in equation (4)). The other is the use of the airborne monitor that limits the threatening ionosphere fronts to those unobserved by the ground and airborne monitors. In contrast, lacking the airborne monitor, conventional single-frequency LAAS is threatened by all ionosphere fronts unobserved by the ground monitor. The further performance improvement by the enhanced system is obviously caused by adding the Delay-based algorithm.

Another interest is to evaluate the sensitivity of these two systems to more severe ionosphere threats. The threat space for CAT III LAAS is still under development; hence, it is worthwhile to simulate the availability for an expanded threat space. We expanded the maximum gradient from 400 mm/km to 500 mm/km and then to 600 mm/km. Note that these gradients correspond to 2-meter, 2.5-meter, and 3-meter differential errors at the decision point. The results are given in Figure 20, in which the subplots in the first row show the availability for 10-meter VAL, and the subplots in the second row show the VAL to obtain 99.999% availability. As shown in the figure, the enhanced system (with a 1000-second time constant) keeps high availability for the enlarged ionosphere gradients, while the baseline system loses significant availability. Similarly, the enhanced system keeps VAL less than 26 m regardless of gradients, while the baseline system requires over 30-meter VAL for the 600 mm/km gradient in some airports.

Table 3: VAL to obtain 99.9% and 99.999% availability
The top value in each cell is VAL needed to obtain 99.9% availability, and the bottom value is VAL needed to obtain 99.999% availability.

	Memphis	LA	NY
Baseline	16.5 m 24.5 m	11.0 m 19.0 m	9.5 m 26.5 m
Enhanced (τ: 1000 s)	14.5 m 23.0 m	9.5 m 17.0 m	9.0 m 25.0 m

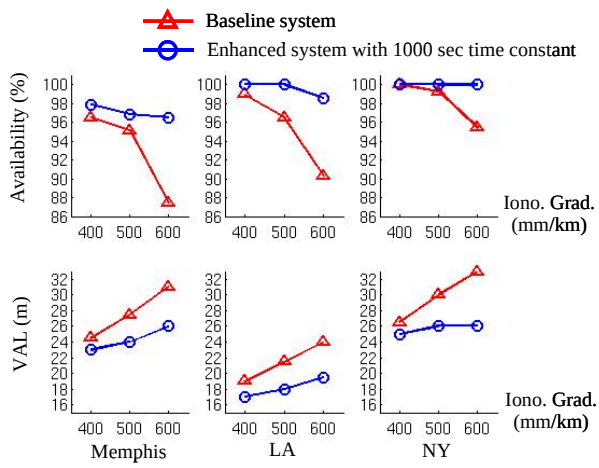

Figure 20: Simulations with expanded threat space

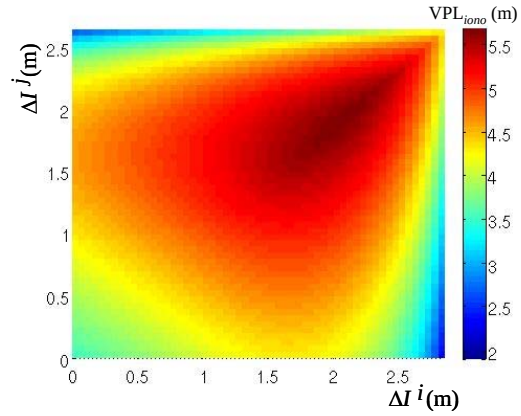

Figure 21: Distribution of VPL$_{iono}$

This simulation demonstrates the robustness of the Delay-based algorithm against ionosphere threats. This robustness can be explained by examining the relationship between the differential range error and VPL$_{iono}$. Although the Delay-based algorithm is insensitive to small differential range errors, gradients of 400 mm/km are marginally detectable, and gradients of more than 500 mm/km are easily detectable. Easier detection corresponds to smaller P_{md}, and the smaller the P_{md} becomes, the more the random part of VPL$_{iono}$ is deflated. At some point, the deflation of the random part surpasses the inflation of the bias part in the computation of VPL$_{iono}$ (see equation (32)); consequently, the VPL$_{iono}$ is upper bounded. This mechanism is clearly shown in Figure 21. This plot shows how VPL$_{iono}$ varies according to the differential range errors on two particular satellites (satellites i and j). The VPL$_{iono}$ hits the ceiling around ΔI^i of 2 m and ΔI^j of 2 m and does not increase for larger errors. This property results in the robustness of the Delay-based algorithm to severe ionosphere conditions.

Although the simulation results are encouraging, limitations of the study should be considered. The most important issue might be the adequacy of the noise model of the Delay-based algorithm. Based on the theory discussed in Subsection 5.4, we assumed the noise level is reduced by a factor of $\sqrt{10}$ by employing the 1000-second time constant. However, the ideal noise reduction is not guaranteed in practice. Evaluating the noise model is an important future task. Also, it is debatable whether the 1000-second time constant would be acceptable for practical applications. Further analysis will be needed to evaluate the impact of the long time constant.

Another issue is the prior probability of ionosphere anomalies. We set P_{iono} to 1 due to the lack of the statistical knowledge about the anomalies; however, this value might be overly conservative. If further research provides plausible evidence for a reduced prior probability, higher availability will be obtained.

8. CONCLUSION AND ONGOING WORK

This paper has introduced two algorithms to detect satellites affected by anomalous ionosphere fronts: the Rate-based algorithm and the Delay-based algorithm. The Rate-based algorithm is a very sensitive detector but suffers from a particular undetectable condition. The Delay-based algorithm is an algorithm that can detect all anomalous situations but is not very sensitive. Combining these algorithms, we have formulated a new VPL accounting for the ionosphere anomalies in a dual-frequency LAAS system.

An important issue remaining from this study is how best to integrate the monitoring algorithms into hybrid dual-frequency LAAS. In this study we combined the algorithms with DFree LAAS only. Hence, we will continue to work on incorporating the monitor into the hybrid system and optimizing the resulting system. Note that the hybrid system adds the option of switching between DFree and IFree to the existing options of the satellite exclusion and VPL inclusion studied in this paper.

Through the analysis presented in this paper, we have quantitatively evaluated the proposed algorithms. Simulations have shown that DFree LAAS could achieve high availability by using only the Rate-based algorithm, given an ionosphere threat space only slightly larger than that used in CAT I LAAS. However, once that threat space was expanded, the DFree system lost significant availability. By contrast, enhanced monitoring for DFree LAAS using two algorithms showed considerable robustness against the expansion of the threat space. Because the ionosphere threat space may be re-evaluated for CAT III to reflect the stricter integrity risk at the 10^{-9}

level, this additional robustness is very attractive in the development of CAT III LAAS.

ACKNOWLEDGEMENTS

The authors would like to thank several people who helped with this paper and the work that it covers, including Ming Luo, Jiyun Lee, Seebany Datta-Barua, and Young Shin Park. The authors would also like to thank the Federal Aviation Administration LAAS Program Office for supporting this research. The opinions discussed in this paper are those of the authors and do not necessarily represent those of FAA or other affiliated agencies.

REFERENCES

[1] M. Luo, S. Pullen, et al., "Ionosphere Threat to LAAS: Updated Model, User Impact, and Mitigations," *Proceedings of ION GNSS 2004*, Long Beach, CA., Sept. 21-24, 2004.

[2] T. Walter, S. Datta-Barua, et al., "The Effects of Large Ionospheric Gradients on Single Frequency Airborne Smoothing Filter for WAAS and LAAS," *Proceedings of ION National Technical Meeting*, San Diego, CA., January, 2004

[3] H. Konno, S. Pullen, et al., "Evaluation of Two Types of Dual-Frequency Differential GPS Techniques under Anomalous Ionosphere Conditions," *Proceedings of ION National Technical Meeting*, Monterey, CA., Jan. 18-20, 2006.

[4] P. Hwang, G. McGraw, J. Bader, "Enhanced Differential GPS Carrier-Smoothed Code Processing Using Dual-Frequency Measurements," *Navigation*. Vol. 46, No. 2, Summer 1999, pp. 127-137.

[5] G. McGraw, P. Young, "Dual Frequency Smoothing DGPS Performance Evaluation Studies," *Proceedings of ION National Technical Meeting*, San Diego, CA., Jan. 24-26, 2005.

[6] G. Xie, "Optimal On-Airport Monitoring of the Integrity of GPS-Based Landing Systems," *Ph.D. Dissertation*, Stanford University, March, 2004.

[7] *Algorithm Description Document for the Code-Carrier Divergence Monitor of the Local Area Augmentation System*. November 2005, Illinois Institute of Technology: Chicago, Illinois.

[8] H. Konno, S. Pullen, et al., "Analysis of Ionosphere Gradient Using Japan GEONET Data," *Proceedings of ION National Technical Meeting*, San Diego, CA., Jan. 24-26, 2005.

[9] B. Wilson, et al., "New and Improved The Broadcast Interfrequency Biases," *GPS World* Sept., 1999, pp. 56-66.

[10] J. Lee, M. Luo, et al., "Position-Domain Geometry Screening to Maximize LAAS Availability in the Presence of Ionosphere Anomalies," *Proceedings of ION GNSS 2006*, Fort Worth, TX., Sept. 26-29, 2006.

[11] L. Gratton, B. Pervan, "Airborne and Ground Monitors for Ionospheric Front Detection for the Local Area Augmentation System Using Carrier Phase Measurments," *Proceedings of ION GNSS 2005*, Long Beach, CA., Sept. 13-16, 2005.

[12] *Minimum Aviation System Performance Standards for Local Area Augmentation System (LAAS)*. Washington, D.C., RTCA SC-159, WG-4A, DO-245A, Dec. 9, 2004.

[13] H. Konno, "Analysis of Ionosphere Anomaly Wave Front Impacts on Multiple Satellites," Stanford University, Dept. of Aeronautics and Astronautics, Unpublished Manuscript, October 20, 2006 (forthcoming). http://waas.stanford.edu/research/laas.htm

[14] G. McGraw, T Murphy, *et al*., "Development of the LAAS Accuracy Models," *Proceeding of ION GPS 2000*, Salt Lake City, UT., Sept. 19-22, 2000.

[15] J. Rife, S. Pullen, "The Impact of Measurement Biases on Availability for CAT III LAAS," *Proceedings of ION Annual Meeting*, Cambridge, MA., June, 2005.

[16] *Global Positioning System Standard Positioning Service Performance Standard*. Washington, D.C., U.S. Department of Defense, October 2001. http://www.navcen.uscg.gov/gps/geninfo/2001SPSPerformanceStandardFINAL.pdf